Materials Research Bulletin 99 (2018) 196–203

Contents lists available at ScienceDirect

Materials Research Bulletin

journal homepage: www.elsevier.com/locate/matresbu

Synergistic effect of hierarchical SnO_2 nanorods/Fe_2O_3 hexahedrons with enhanced performance as lithium ion battery anodes

Tuo Xin[1], Feiyu Diao[1], Chen Li, Honglei Feng, Guiju Liu, Jiajia Zou, Yanhua Ding, Bing Liu*, Yiqian Wang*

College of Physics, Qingdao University, No. 308 Ningxia Road, Qingdao, 266071, People's Republic of China

ARTICLE INFO

Keywords:
Lithium-ion batteries
Hierarchical SnO_2/Fe_2O_3 nanocomposites
Synergistic effect
Fully reversible conversion reaction

ABSTRACT

Hierarchical SnO_2-Fe_2O_3 nanocomposites composed of SnO_2 nanorods and Fe_2O_3 hexahedrons are successfully prepared by a two-step hydrothermal method. The lithium ion batteries (LIBs) based on as-synthesized products are fabricated to investigate their electrochemical performance. As an anode material for LIBs, SnO_2-Fe_2O_3 nanocomposites deliver a high capacity of 1022 mAh g^{-1} at 100 mA g^{-1} after 100 cycles. The cycling stability and rate performance of the nanocomposites are significantly improved. The enhanced performances benefit from the synergistic effect of SnO_2 nanorods and Fe_2O_3 hexahedrons. The iron (Fe) nanoparticles reduced from Fe_2O_3 not only facilitate the conversion reaction of SnO_2, resulting in the high capacity, but also increase the conductivity of the material. In addition, SnO_2 serves as a matrix to protect Fe_2O_3 from agglomeration, and the hierarchical structure effectively buffers volume changes, thus enhancing the cycling life of LIBs.

1. Introduction

Owing to the emergence of various electric vehicles and portable electronic devices, the demand for sustainable resources and clean energy has been growing. Lithium-ion batteries (LIBs), as one of the highly-efficient energy storage devices, have attracted great attention due to their high energy density, power density and long cycle life. [1–6] At present, graphite materials are the most commonly-used anode materials in commercial LIBs. However, the theoretical capacity of 372 mAh g^{-1} does not meet the growing demand for high performance LIBs. [7–9] Therefore, the construction of novel anode materials with high capacities is an urgent task for developing new type LIBs. Many new anode materials have attracted much interest due to their unique properties. For example, silicon (Si) is expected to be a promising high-capacity anode of LIBs. [10] Si nanostructures have been combined with graphene to improve their electrochemical performance. [11,12] Recently, metal oxides have been extensively investigated as anode materials due to their high theoretical capacity. [13,14]

Among various metal oxides, tin dioxide (SnO_2) and hematite (Fe_2O_3) are versatile semiconductor materials which are commonly used in LIBs [15], gas sensors [16,17] and solar cells [18,19]. Recently, SnO_2 and Fe_2O_3 are considered to be potential alternatives to graphite in the LIBs because of their high theoretical capacity, non-toxicity and safety. [20,21] Despite these advantages, SnO_2 and Fe_2O_3 still undergo intense volume expansion and severe pulverization during the charge-discharge process as anode materials for LIBs, resulting in poor electrochemical performance. [22–24] Up to now, much effort has been directed towards solving these problems of anode materials based on SnO_2 and Fe_2O_3. For example, various novel structures such as SnO_2 hollow nanostructures [13], Fe_2O_3 nanotubes [25], and hierarchical Fe_2O_3 microspheres [5] were synthesized to accommodate the volume variation during the charge-discharge process. To improve the electrochemical performance of SnO_2 and Fe_2O_3, hybridizing metallic oxides with carbonaceous materials or doping with nitrogen are effective ways to increase the conductivity of anode materials and shorten Li^+ diffusion length during the discharge-charge process. [26,27] Recently, many different active-material heterostructures such as SnO_2/CuO [28], CuO—Cu_2O [29], Fe_2O_3-TiO_2 [30], TiO_2-TiN [31] have been reported to possess enhanced electrochemical performance. The synergistic effect of two different active materials has been reported, which not only significantly improves the lithium storage properties but also enhances the stability of the anode materials. [32–35] However, it still remains a great challenge to fabricate a stable two-metal-oxide composite anode with a high reversible capacity and an excellent rate performance.

Herein, we report a two-step hydrothermal method for fabrication of hybrid hierarchical SnO_2-Fe_2O_3 nanocomposites and evaluate their electrochemical properties as anode materials for LIBs. The battery

---

* Corresponding authors.
E-mail addresses: bing_liu@qdu.edu.cn (B. Liu), yqwang@qdu.edu.cn (Y. Wang).

[1] These authors contributed to this work equally.

https://doi.org/10.1016/j.materresbull.2017.11.021
Received 10 July 2017; Received in revised form 1 October 2017; Accepted 9 November 2017

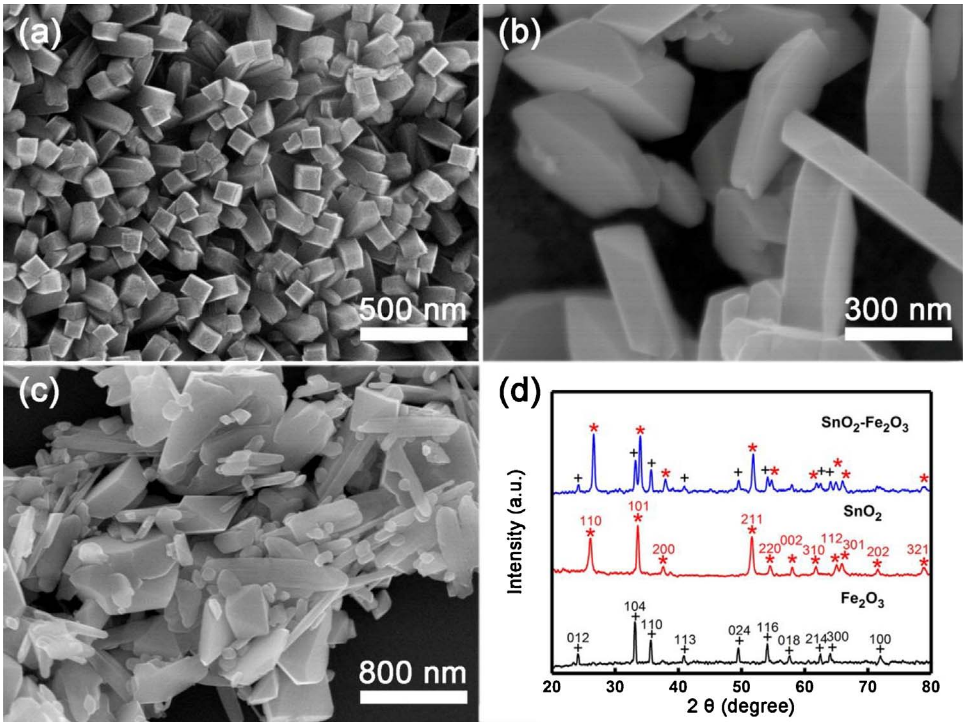

Fig. 1. Typical SEM images of as-synthesized SnO_2 nanorods (a), Fe_2O_3 hexahedrons (b), and SnO_2-Fe_2O_3 nanocomposites (c); (d) The corresponding XRD patterns.

delivers a capacity of 1022 mAh g^{-1} at a current density of 100 mA g^{-1} after 100 cycles. Compared with bare SnO_2 nanorods and Fe_2O_3 hexahedrons, the SnO_2-Fe_2O_3 nanocomposites exhibit larger capacity, better cycle performance and higher rate performance. The outstanding electrochemical performance of SnO_2-Fe_2O_3 nanocomposites can be attributed to the synergistic effect of two metal oxides.

2. Experimental

All chemicals were of analytical grade and used as received. Distilled water was used throughout the whole experiment.

2.1. Synthesis of SnO_2 nanorods

SnO_2 nanorods were synthesized by a simple hydrothermal method. Typically, 20 mL of 0.75 mol L^{-1} NaOH aqueous solution was added to 20 mL of 0.075 mol L^{-1} $SnCl_4·5H_2O$ ethanol solution under vigorous stirring and subjected to ultrasonic treatment for 5 min. The mixture solution was then transferred into a 100 mL Teflon-sealed autoclave and maintained at 180 °C for 18 h. Subsequently, the resultant precipitates were collected by centrifugation and washed with distilled water and ethanol several times, and then dried at 60 °C for 12 h. Finally, the dry powder was annealed in air at 600 °C for 3 h in a tube furnace to obtain final products.

2.2. Synthesis of Fe_2O_3 hexahedrons

0.48 mmol $FeCl_3·6H_2O$ and 15 mmol NaOH were dissolved in 20 mL and 40 mL of distilled water, respectively. Thereafter, NaOH solution was dropped into the $FeCl_3$ solution under stirring to obtain a homogeneous solution. The mixture was transferred to a 100 mL Teflon sealed autoclave and heated at 180 °C for 18 h. The obtained sample was rinsed with distilled water and ethanol for several times, and dried in air at 60 °C for 12 h. Afterwards, the obtained products were annealed in air at 600 °C for 3 h.

2.3. Synthesis of SnO_2-Fe_2O_3 nanocomposites

3.2 mmol of the synthesized SnO_2 powder was dispersed in a solution of 80 mL of ethanol/water (1:1 vol ratio) and then continuously stirred for 10 min and ultrasonicated for 10 min. Then, 0.96 mmol of $FeCl_3·6H_2O$ was added into the suspension under stirring and 30 mmol NaOH was dissolved in 40 mL distilled water. NaOH solution was added dropwise to the suspension and the resulting mixture was placed in a 100 mL Teflon-sealed autoclave. Thereafter, the autoclave was heated at 180 °C for 18 h. After cooling to room temperature, the resultant precipitates was centrifuged, washed several times with distilled water and ethanol, and dried in oven at 60 °C for 12 h. Finally, the resulting sample was further heated in air at 600 °C for 3 h.

2.4. Material characterization

The morphologies of the as-synthesized samples were characterized by scanning electron microscope (SEM, Hitachi S-4800) and the crystal structures of the samples were analyzed by SmartLab XRD with Cu-Kα1 radiation ($\lambda = 1.5406$ Å). Selected-area electron diffraction (SAED) pattern, bright-field (BF) images and high-resolution transmission electron microscopy (HRTEM) images were obtained on a JEOL JEM2100F transmission electron microscope (TEM) with an accelerating voltage of 200 kV. X-ray photoelectron spectroscopy (XPS) was performed on a Thermo Scientific ESCALAB 250Xi instrument with monochromatic Al Kα radiation ($h\nu = 1486.6$ eV) at ultrahigh vacuum (below 10^{-8} Pa). The binding energies were calibrated using C 1 s peak (284.8 eV) as a reference.

2.5. Electrochemical measurements

The electrochemical test was carried out in a CR2025-type coin cell (20 mm in diameter and 2.5 mm in thickness) with lithium metal as a counter electrode at room temperature. The working electrode was fabricated by mixing the as-prepared active materials (SnO_2 nanorods, Fe_2O_3 hexahedrons and SnO_2-Fe_2O_3 nanocomposites) with carbon black and water-soluble sodium alginate (SA) in a weight ratio of 70:15:15 (wt.%) onto a pure copper foil. The electrodes were dried in a

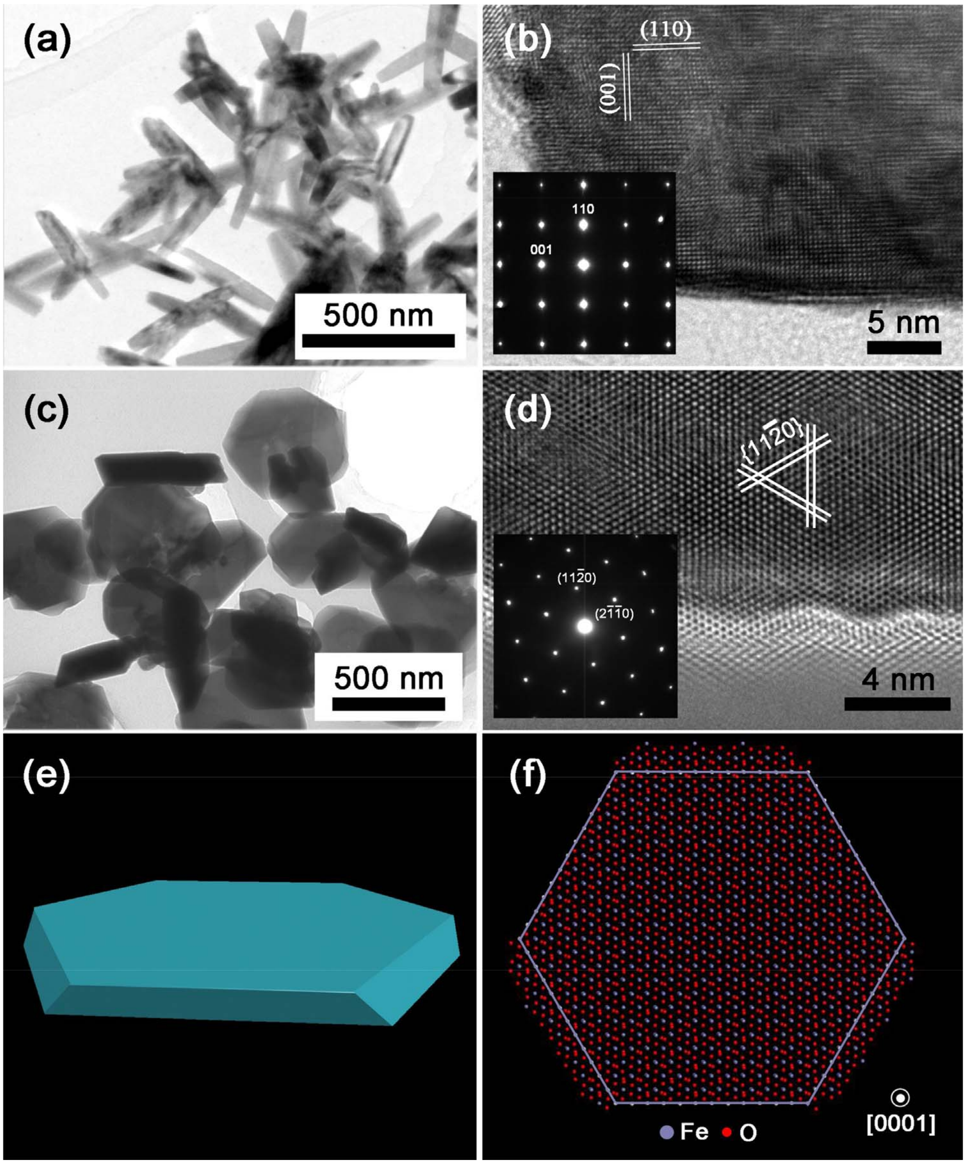

Fig. 2. (a) Typical BF TEM image of SnO_2 nanorods; (b) HRTEM image of an individual nanorod viewed along the [1$\bar{1}$0] direction. The lower-left corner inset is the corresponding SAED pattern; (c) Typical BF TEM image of Fe_2O_3 hexahedrons; (d) Typical HRTEM image for the Fe_2O_3 hexahedrons viewed along the [0001] direction. Inset is the SAED pattern; (e) Schematic model of an ideal Fe_2O_3 hexahedron; (f) Schematic model of an ideal Fe_2O_3 hexahedron projected along the [0001] direction.

vacuum oven at 120 °C for 12 h and the cells were assembled in a glove box filled with argon with a moisture and oxygen concentration of less than 1 ppm. The mass loadings of SnO_2, Fe_2O_3 and SnO_2-Fe_2O_3 composites for cell testing were 1.5 mg, 1.4 mg and 1.5 mg, respectively. The electrolyte consisted of 1 M $LiPF_6$ solution of ethylene carbonate (EC)/dimethyl carbonate (DMC)/diethyl carbonate (DEC) (1:1:1 in volume). The electrochemical performances were tested on a LAND CT2001 battery test system in a voltage range of 0.01 V-3.00 V at room temperature. Cyclic voltammetry (CV) measurements (over the potential range of 0.01 V-3.00 V at a scan rate of 0.1 mV s^{-1}) and electrochemical impedance spectroscopy (EIS) tests were performed on a Metrohm Autolab electrochemical workstation (PGSTAT 302N) with a frequency range from 100 kHz to 0.01 Hz.

3. Results and discussion

Fig. 1 displays typical SEM images and XRD patterns of the three different nanostructures, respectively. It can be seen from Fig. 1a that SnO_2 nanorods show relatively uniform quadrangular shape with a length of ~ 500 nm and a width of ~ 80 nm. Fig. 1b is a typical SEM image of the as-synthesized Fe_2O_3, in which these nanocrystals are hexahedral. The average size of hexagonal platelets is about 200 nm in thickness and the edge length is about 500 nm, which can be tunable with the sample concentration. Careful examination shows that the six side faces of the Fe_2O_3 hexahedrons are all trapezoidal and the direction of two adjacent sides is opposite. Fig. 1c shows a typical SEM image of SnO_2-Fe_2O_3 nanocomposites. From this image, it can be seen that the hierarchical structures are assembled with SnO_2 nanorods and Fe_2O_3 hexahedrons. SnO_2 still keeps the rod shape and the size of the nanorods does not change. After the SnO_2 growth, the newly-formed Fe_2O_3 aggregates into hexahedrons with a thickness similar to the individually-synthesized ones. Fig. 1d shows the XRD patterns of the as-synthesized products. For SnO_2 nanorods and Fe_2O_3 hexahedrons, all the diffraction peaks can be indexed to tetragonal rutile SnO_2 (JCPDS no.: 41-1445) and rhombohedral Fe_2O_3 (JCPDS no.: 33-0664), respectively. In particular, all the diffraction peaks for SnO_2-Fe_2O_3 nanocomposites are in good agreement with those of tetragonal rutile SnO_2 and rhombohedral Fe_2O_3. No notable peak of impurities can be detected, which indicates that three different nanostructures have high purity and good crystallinity.

The microstructures of the as-synthesized samples were extensively examined by TEM. Fig. 2a shows a typical BF TEM image of SnO_2 nanorods. It can be seen that the SnO_2 nanostructures consist entirely of uniform nanorods, in agreement with the SEM result (Fig. 1a). Fig. 2b

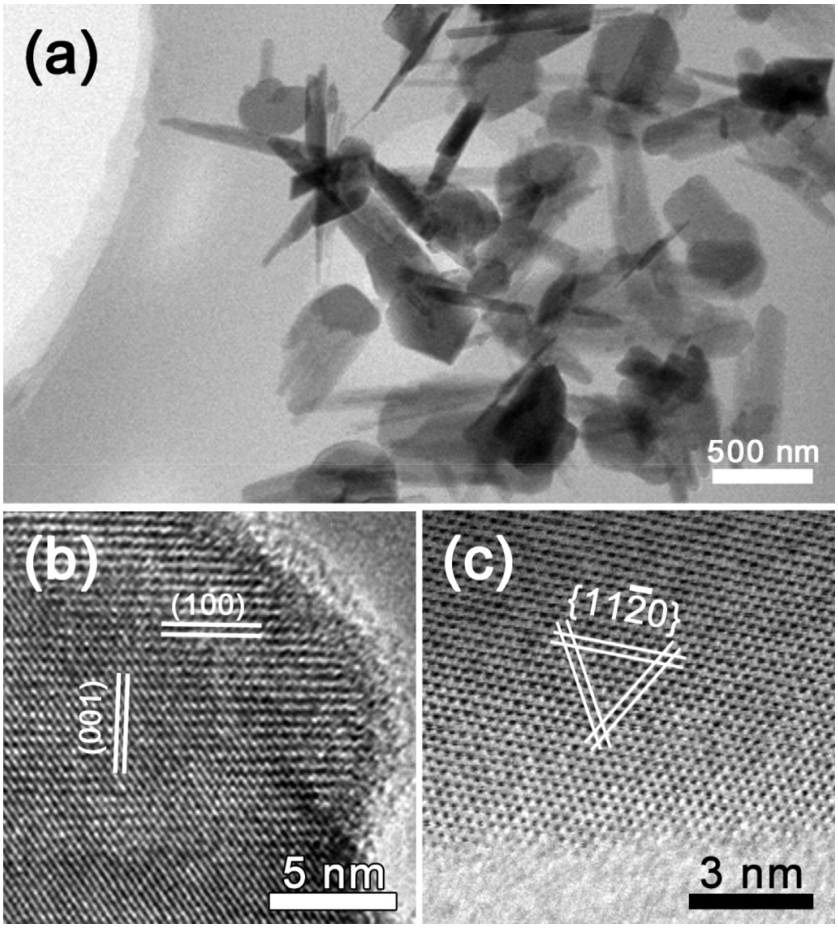

Fig. 3. (a) Typical BF TEM image of the hierarchical SnO_2-Fe_2O_3 nanocomposites; (b) Typical HRTEM image for a SnO_2 nanorod viewed along the [010] direction; (c) Typical HRTEM image for a Fe_2O_3 hexahedron viewed along the [0001] direction.

shows a typical HRTEM image of the SnO_2 nanorods. The crystal lattice spacings are measured to be 3.35 Å and 3.15 Å, corresponding to the interplanar spacings of (110) side facets and (001) top facets of the nanorods, respectively. The lower-left corner inset is the corresponding SAED pattern, which reveals that the SnO_2 NRs are single crystals and can be indexed to [1$\bar{1}$0] zone-axis of tetragonal SnO_2. Fig. 2c presents a typical BF TEM image, illustrating that Fe_2O_3 nanostructures consist of hexahedrons. Fig. 2d shows a typical [0001] zone-axis HRTEM image of a single Fe_2O_3 hexahedron, where the {11$\bar{2}$0} lattice spacing is 2.51 Å, consistent with that of Fe_2O_3. The inset in Fig. 2d is the corresponding SAED pattern, which can be indexed to rhombohedral Fe_2O_3. Based on the SEM and TEM images, we present a model of an ideal hexahedral Fe_2O_3, as shown in Fig. 2e. To determine the exposed facets of Fe_2O_3 hexahedrons, an atomic model of the ideal Fe_2O_3 hexahedron enclosed by two {0001} top facets and six {11$\bar{2}$3} trapezoid facets projected along the [0001] direction was built, as shown in Fig. 2f. It can be seen that the outline of the Fe_2O_3 hexahedrons in Fig. 2e is consistent with the atomic model, which confirms that the Fe_2O_3 hexahedrons possess exposed facets of {0001} and {11$\bar{2}$3}.

Fig. 3a shows a typical BF TEM image, illustrating that the hierarchical SnO_2-Fe_2O_3 nanocomposites consist of SnO_2 nanorods and Fe_2O_3 hexahedrons. Fig. 3b shows a typical [010] zone-axis HRTEM image of the SnO_2 nanorod in SnO_2-Fe_2O_3 nanocomposites. The crystal lattice spacings measured from the HRTEM images are 3.18 Å and 4.73 Å, respectively, which correspond to the interplanar spacings of {001} and {100} planes of rutile SnO_2. Fig. 3c shows a typical [0001] zone-axis HRTEM image of the Fe_2O_3 hexahedrons in the nanocomposites. The crystal lattice spacing is 2.51 Å, which is in accordance with the interplanar spacing of {11$\bar{2}$0} of Fe_2O_3.

To gain the detailed chemical compositions of as-synthesized SnO_2-Fe_2O_3 nanocomposites, XPS spectra were performed, as shown in Fig. 4. The peak located at 284.8 eV can be indexed to C 1*s* spectrum (Fig. 4a), demonstrating the existence of benchmark carbon. Moreover, for the O 1*s* spectrum in Fig. 4b, the peak at 529.9 eV indicates the presence of O^{2-}, which forms oxides with Sn and Fe. [30] In Fig. 4c, there are two peaks in the Sn 3*d* region. The peak located at 486.5 eV arises from Sn $3d_{5/2}$, and the other one located at 494.9 eV corresponds to the Sn $3d_{3/2}$. [36] The splitting gap between Sn $3d_{5/2}$ and Sn $3d_{3/2}$ core levels is 8.4 eV, indicating a normal state of Sn^{4+} in the SnO_2-Fe_2O_3 nanocomposites. For Fe 2*p* spectrum in Fig. 4d, the peaks of Fe $2p_{3/2}$ and Fe $2p_{1/2}$ appeared at the binding energies of 710.9 eV and 724.2 eV, respectively. Two satellite peaks located at 716.5 eV and 728.6 eV are consistent with those of Fe_2O_3 in previous reports. [30] This result agrees well with the XRD patterns. Furthermore, the calculation of peak areas in Sn 3*d* and Fe 2*p* core level spectra gives an Sn/Fe atomic ratio of about 1:2, suggesting that the molar ratio of SnO_2 and Fe_2O_3 is about 1:1 in the as-prepared product.

The as-synthesized products were used as anode materials for LIBs to elucidate the electrochemical properties. As we all know, the lithium storage mechanism of SnO_2 involves a two-step reaction,

$$SnO_2 + 4Li^+ + 4e^- \rightarrow Li_2O + Sn \quad (1)$$

$$Sn + xLi^+ + xe^- \leftrightarrow Li_xSn\ (0 \le x \le 4.4) \quad (2)$$

Normally, the conversion reaction Eq. (1) is generally considered irreversible and does not contribute to the reversible capacity. Eq. (2) is widely considered to be reversible and the theoretical capacity of 792 mAh g^{-1} for SnO_2 is calculated mainly based on Eq. (2). [37] Recently, Eq. (1) is proved to be completely reversible and can increase the theoretical specific capacity of SnO_2. [37] Therefore, the overall electrochemical reaction of SnO_2 should be expressed as:

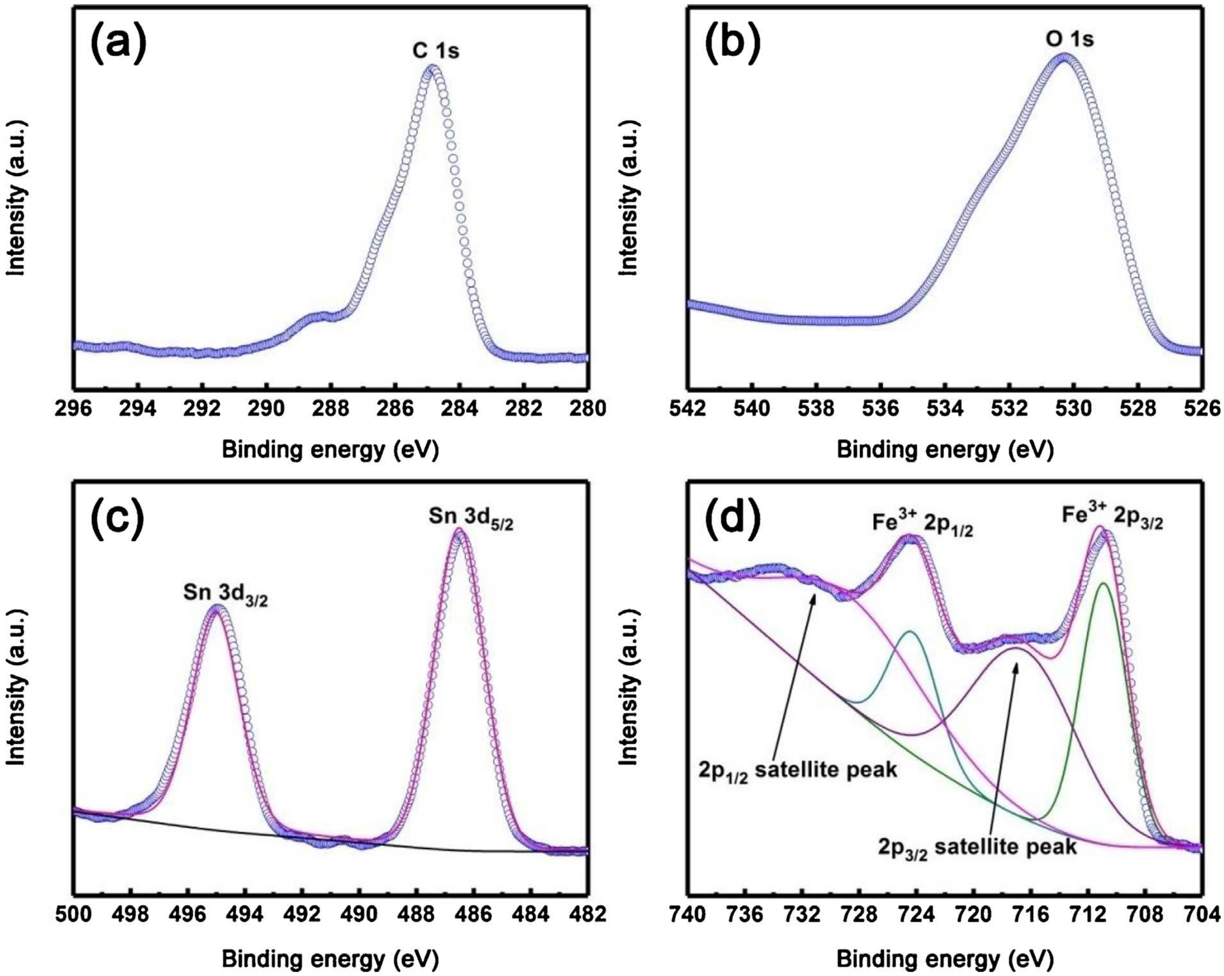

Fig. 4. XPS core level spectra of (a) C 1*s*, (b) O 1*s*, (c) Sn 3*d* and (d) Fe 2*p* for SnO_2-Fe_2O_3 nanocomposites.

$$SnO_2 + 8.4Li^+ + 8.4e^- \leftrightarrow Li_{4.4}Sn + 2Li_2O \tag{3}$$

Hence, the theoretical capacity of SnO_2 increases from 792 mAh g^{-1} to 1494 mAh g^{-1}, which is about four times higher than that of graphite. [14]

When Fe_2O_3 is used as an anode material for LIBs, there is only one step conversion reaction. The electrochemical process can be described using the equation [29] as follows,

$$Fe_2O_3 + 6Li^+ + 6e^- \leftrightarrow 2Fe + 3Li_2O \tag{4}$$

The theoretical capacity of Fe_2O_3 is calculated to be 1007 mAh g^{-1}.

To study the phase changes and ion diffusion process of the electrode materials in the charge-discharge process, CV curves of three different nanostructures were carried out. Figs. 5a–c demonstrate the first six CV cycles of SnO_2 nanorods, Fe_2O_3 hexahedrons and SnO_2-Fe_2O_3 nanocomposites in the potential range of 0.01 V-3.00 V at a scan rate of 0.1 mV s^{-1}, respectively. In Fig. 5a, a significant reduction peak at around 0.63 V (versus Li/Li^+) is observed in the first cycle and disappears in subsequent cycles, which could be ascribed to the formation of the solid electrolyte interface (SEI) due to the electrolyte degradation, resulting in a large initial irreversible capacity. The reduction peak A (0.13 V) and the oxidation peak A′ (0.53 V) correspond to the reversible alloying reaction of the Sn alloy [Eq. (2)]. Furthermore, two pairs of redox peaks located at B′ (1.40 V), B″ (1.87 V) and B_1 (0.90 V), B_2 (1.12 V) could be ascribed to the phase transition from Li_xSn alloy and Li_2O to SnO_2, described in Eq. (1). [37,38] In the subsequent reduction and oxidation scans, the CV curves almost overlap, implying good reversibility of the electrochemical reactions. Fig. 5b shows the first six CV curves of Fe_2O_3 hexahedrons. Consistent with those reported in literature, [39,40] one pair of distinct redox current peaks could be clearly identified from the CVs. A sharp reduction peak C (0.40 V) is observed in first scan, which could be assigned to be the conversion of Fe_2O_3 to Fe and the formation of amorphous Li_2O described in Eq. (4). The subsequent scans show a distinct decrease in the peak intensity, indicating a high degree of irreversibility of the conversion reaction. In addition, the oxidation peak C′ (1.72 V) could be attributed to the formation of Fe^{3+} from Fe^0 and exhibited insignificant change in the first six cycles, indicating good stability of Fe_2O_3 hexahedrons. Compared with the SnO_2 nanorods and Fe_2O_3 hexahedrons, the CV profiles of SnO_2-Fe_2O_3 nanocomposites are shown in Fig. 5c. A reduction peak at around 0.65 V (versus Li/Li^+) is observed in the first cycle and disappears in subsequent cycles, which results from the formation of SEI film due to irreversible electrolyte degradation. Moreover, it can be seen from the curves that the reduction peak A (0.18 V) and oxidation peak A′ (0.54 V) correspond to reversible alloying reaction of the Sn alloy. The reduction peak C (0.81 V) and oxidation peak C′ (1.94 V) are attributed to the conversion of Fe_2O_3, as expressed in Eq. (4). The peak B (1.20 V) may be assigned to the reduction of SnO_2 to Sn and the simultaneous formation of Li_2O in Eq. (1). The two oxidation peaks B′ (1.32 V) and B″ (1.65 V) correspond to the excellent reversibility of the conversion reaction of SnO_2, as described in Eq. (1). As shown in Fig. 5c, the current density and the integral area of the SnO_2-Fe_2O_3 nanocomposites are larger than that of SnO_2 nanorods or Fe_2O_3 hexahedrons, which indicates that the SnO_2-Fe_2O_3 nanocomposites have enhanced electrochemical activity.

Fig. 5d shows the first charge-discharge curves of three different

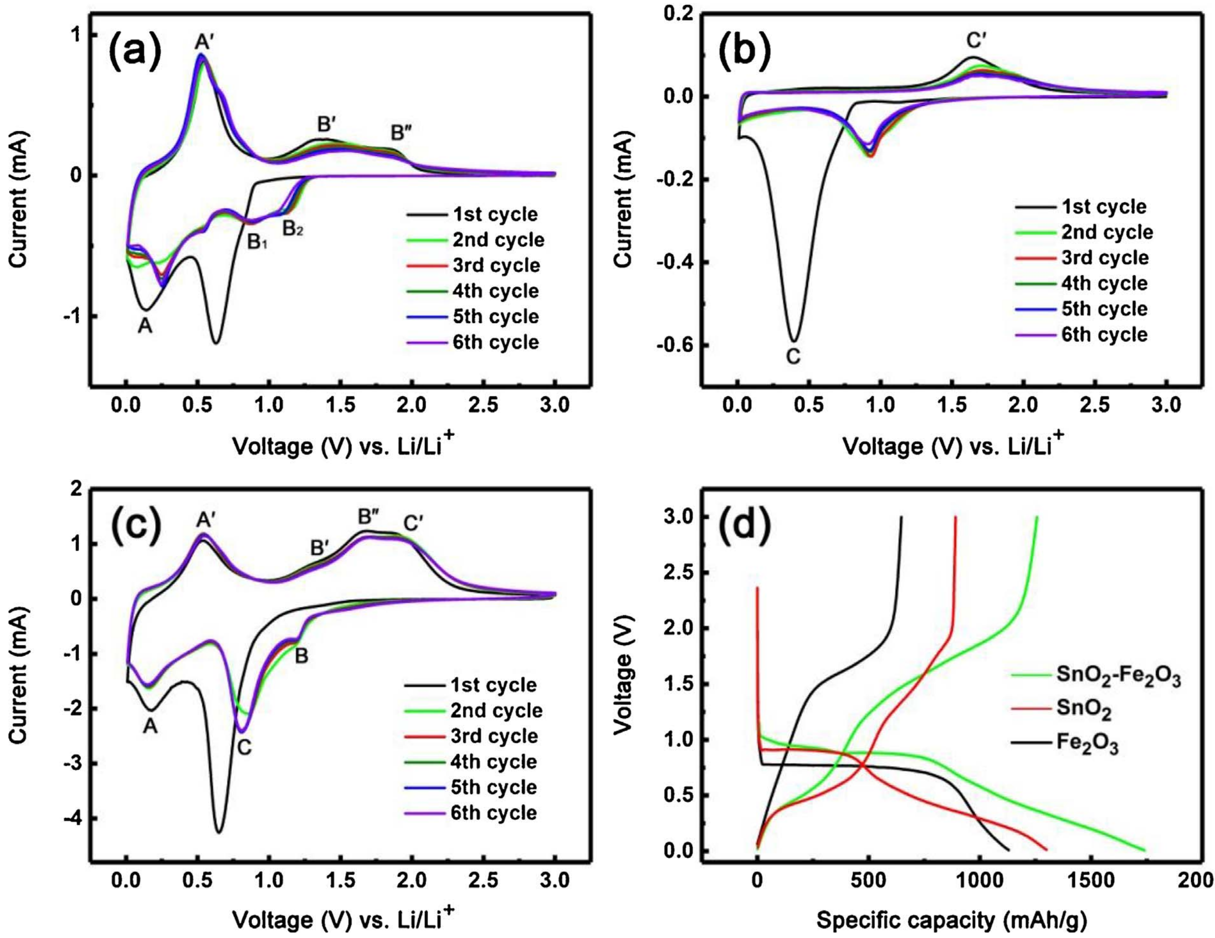

Fig. 5. (a) Cyclic voltammetry curves of SnO_2 nanorods; (b) Cyclic voltammetry curves for Fe_2O_3 hexahedrons; (c) Cyclic voltammetry curves for SnO_2-Fe_2O_3 nanocomposites at 0.1 mV s^{-1}; (d) Initial voltage vs. capacity curves of the SnO_2-Fe_2O_3 nanocomposites at 100 mA g^{-1}.

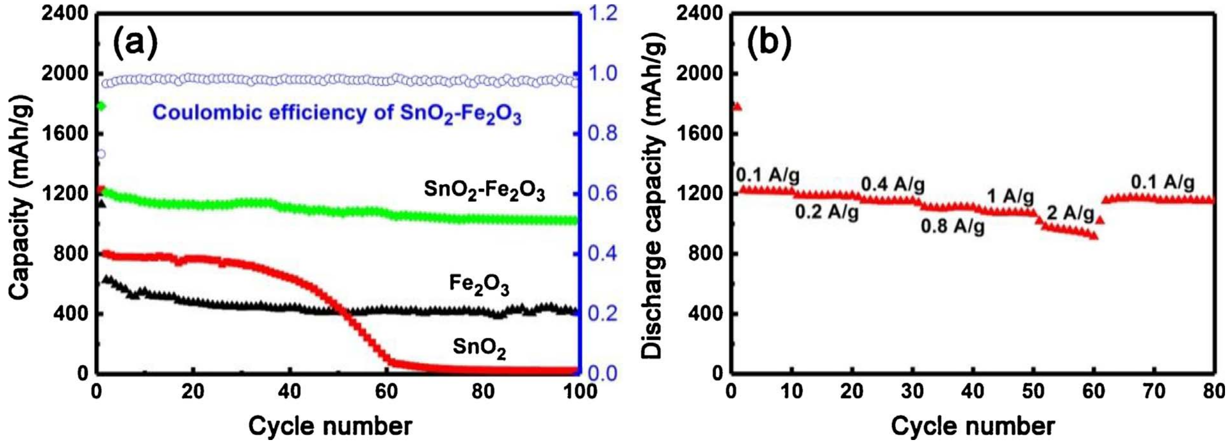

Fig. 6. (a) Comparative cycling performance of as-synthesized SnO_2 nanorods, Fe_2O_3 hexahedrons and SnO_2-Fe_2O_3 nanocomposites at the same current density, 100 mA g^{-1}; (b) Cycle performance of SnO_2-Fe_2O_3 nanocomposites at various current rates.

nanostructures at a current density of 100 mA g^{-1} in the range of 0.01-3.00 V vs. Li/Li^+. Obviously, the discharge process of three different nanostructures could be divided into three stages. At the beginning, the voltage drops rapidly in the first stage. The second stage has a longer discharge platform at about 0.8 V vs. Li/Li^+ and most intercalation reactions occur in this section, which contributes to the most capacity. In the third stage, it can be seen that the voltage drops slowly. The initial discharge and charge capacity of SnO_2-Fe_2O_3 nanocomposites are 1738 and 1256 mAh g^{-1}, respectively, which are much higher than those of SnO_2 nanorods (1296 and 887 mAh g^{-1}) and Fe_2O_3 hexahedrons (1133 and 645 mAh g^{-1}). Three different nanostructures have a large initial capacity loss, which is mainly ascribed to the formation of SEI layer. The initial coulombic efficiency (CE) of SnO_2-Fe_2O_3 nanocomposites anode (72.27%) is higher than that of SnO_2 nanorods (68.44%) or Fe_2O_3 hexahedrons (56.93%). The higher capacity and outstanding CE of SnO_2-Fe_2O_3 nanocomposites suggest that the conversion reaction of SnO_2 is highly reversible due to the introduction of Fe_2O_3 in binary SnO_2-Fe_2O_3 nanocomposites, resulting in a higher

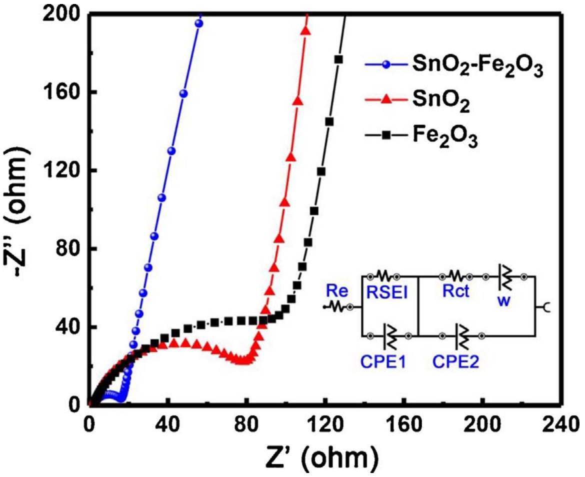

Fig. 7. EIS of SnO_2 nanorods, Fe_2O_3 hexahedrons and SnO_2-Fe_2O_3 nanocomposites. Inset is the equivalent electrical circuit.

capacity.

The cycle performances of three different nanostructures were also evaluated at a current density of $100\ mA\ g^{-1}$, as shown in Fig. 6a. It can be clearly seen that the reversible capacity of SnO_2 nanorod electrode decreases slightly after charging and discharging, and still maintains $636\ mAh\ g^{-1}$ after 40 cycles. However, the capacity of SnO_2 nanorods drops rapidly after 40 cycles and only reserves $55\ mAh\ g^{-1}$ after 100 cycles, indicating that the electrode material has suffered from severe pulverization, which leads to a loss of electrical contact after 50 cycles. For the Fe_2O_3 hexahedrons, it only delivers an average discharge capacity of $435\ mAh\ g^{-1}$ after 100 cycles at $100\ mA\ g^{-1}$, much smaller than the theoretical capacity of Fe_2O_3. Compared with SnO_2 nanorods and Fe_2O_3 hexahedrons, the SnO_2-Fe_2O_3 nanocomposites exhibit a superior discharge capacity and cycling performance. The discharge capacity remains $1022\ mAh\ g^{-1}$ after 100 cycles. The high discharge capacity of the composite material indicates that the conversion reaction in SnO_2 is fully reversible.

The theoretical capacity of SnO_2-Fe_2O_3 nanocomposites can be calculated using the following equation.

$$C_{SnO2\text{-}Fe2O3} = C_{SnO2} \times M_{SnO2} + C_{Fe2O3} \times M_{Fe2O3} \quad (5)$$

where $C_{SnO2\text{-}Fe2O3}$, C_{SnO2} and C_{Fe2O3} correspond to the theoretical capacity of SnO_2-Fe_2O_3 nanocomposites, SnO_2 nanorods and Fe_2O_3 hexahedrons, respectively. M_{SnO2} and M_{Fe2O3} are the molar fractions of SnO_2 and Fe_2O_3 in the SnO_2-Fe_2O_3 nanocomposites, respectively. The theoretical capacity of SnO_2-Fe_2O_3 nanocomposites is calculated to be $1251\ mAh\ g^{-1}$, and the reserved capacity ($1022\ mAh\ g^{-1}$) is very close to the theoretical capacity. In addition, the corresponding average CE reaches 99.7%, demonstrating the highly reversible Li^+ insertion/extraction kinetics during the cycling process. From the above, the excellent cycling performance can be ascribed to the hierarchical structure of SnO_2-Fe_2O_3 nanocomposites, which can buffer against the volume expansion.

To evaluate the rate performance of SnO_2-Fe_2O_3 nanocomposites, the battery was measured at different current densities. The electrode exhibits good capacity retention at different rates, as shown in Fig. 6b. For example, at a high rate of $2\ A\ g^{-1}$, the SnO_2-Fe_2O_3 nanocomposite electrode can deliver a stable capacity of $957\ mAh\ g^{-1}$, which is higher than the theoretical capacity of graphite-based anode. Notably, an average capacity of $1169\ mAh\ g^{-1}$ is recovered when the current is reduced to $0.1\ A\ g^{-1}$ again, which demonstrates an excellent rate performance of SnO_2-Fe_2O_3 nanocomposites. The little loss of capacity indicates the nanocomposites have a good electrical conductivity at different current densities during the cycling process.

To further understand the excellent electrochemical performance, EIS measurements of three different nanostructures were carried out and the equivalent electrical circuit according to impedance spectrum was fitted, as shown in Fig. 7. It can be seen that the Nyquist plots consist of two semicircles at high and medium frequency, and a straight line at low frequency. The straight line in the low frequency region is related to the Warburg impedance, indicating the solid state diffusion of Li^+ in the electrode. The semicircle in the high frequency region is attributed to the Li^+ migration resistance through SEI layer (R_{SEI}). The semicircle in the medium frequency region corresponds to the charge transfer resistance through electrode/electrolyte (R_{ct}). Apparently, the diameter of the semicircle of SnO_2-Fe_2O_3 nanocomposite electrode (Ω) is much smaller than that of SnO_2 nanorod electrode (Ω) and that of Fe_2O_3 hexahedron electrode (Ω), respectively. The obvious decrease of impedance indicates that the conductivity of the SnO_2-Fe_2O_3 nanocomposites is enhanced. The Li^+ and electrons can transfer more freely through the electrode/electrolyte interface.

To clarify the excellent electrochemical performance of SnO_2-Fe_2O_3 nanocomposites, we studied the detailed microstructure of the electrode materials after 100 cycles at a current rate of $100\ mA\ g^{-1}$, as shown in Fig. 8. From Fig. 8a, it can be seen that the morphology of the composites is destroyed and the electrode pulverization takes place, resulting in the aggregation of the nanoparticles. Fig. 8b shows a typical HRTEM of a single particle, where the lattice spacing is measured to be 2.05 Å, corresponding to interplanar spacing of (110) plane of metallic Fe. A thin SEI layer (~3 nm) can be seen around Fe nanoparticles, which results in the large irreversible loss during the initial two cycles. Fig. 8c presents a typical HRTEM image of SnO_2 after cycling. From this HRTEM image, the crystal lattice spacing is measured to be 2.11 Å, consistent with the interplanar spacing of (210) plane of SnO_2, which indicates the reversibility of the conversion reaction of SnO_2. The

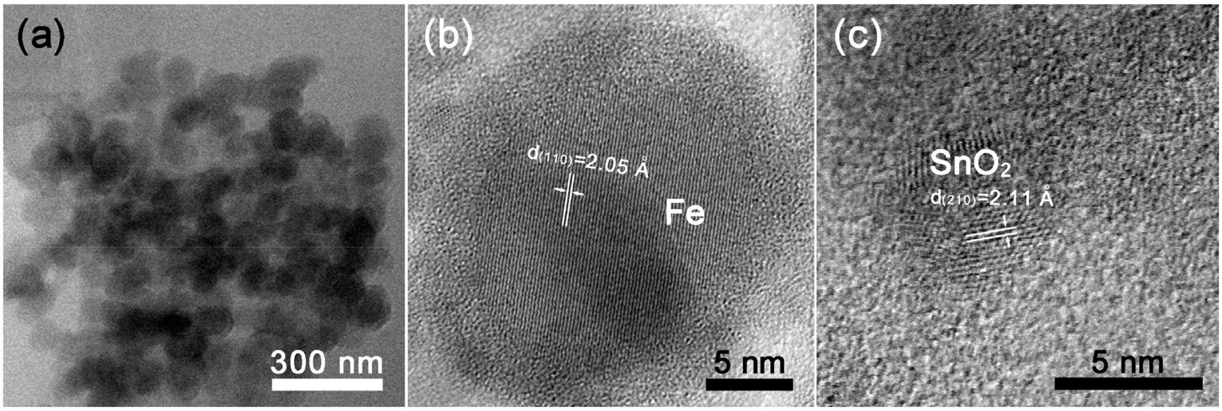

Fig. 8. (a) Representative TEM image of SnO_2-Fe_2O_3 nanocomposite electrode after 100 cycles at $100\ mA\ g^{-1}$; (b and c) Typical HRTEM images of SnO_2-Fe_2O_3 nanocomposite electrode at state of charging to 3.0 V after 100 cycles at $100\ mA\ g^{-1}$.

enhanced electrochemical performance is ascribed to the synergistic effect between SnO_2 nanorods and Fe_2O_3 hexahedrons. It is noted that the reversible formation and decomposition of the Li_2O could be electrochemically driven by metal nanoparticles. [41] Fe nanoparticles reduced from Fe_2O_3 in the discharging process can facilitate the decomposition of Li_2O, which can effectively improve the reversibility of the conversion reaction of SnO_2 ($SnO_2 + 4Li^+ + 4e^- \rightarrow Li_2O + Sn$). In addition, SnO_2 serves as a matrix to protect Fe_2O_3 from agglomeration, thereby improving the cycling performance of LIBs.

4. Conclusions

In summary, we synthesized SnO_2-Fe_2O_3 nanocomposites using a simple two-step hydrothermal method. The SnO_2-Fe_2O_3 nanocomposite electrode shows a high specific capacity, a long cycling life, and an excellent rate performance. The enhanced electrochemical performance is ascribed to the synergistic effect between SnO_2 nanorods and Fe_2O_3 hexahedrons. SnO_2-Fe_2O_3 nanocomposites have a promising potential for anode materials in LIBs. Our work can provide profitable guidance for the design of two distinct metal oxides as anode materials for LIBs.

Acknowledgments

We would like to thank the financial support from the National Key Basic Research Development Program of China (Grant No.: 2012CB722705), the National Natural Science Foundation of China (Grant No.: 10974105), the Natural Science Foundation for Outstanding Young Scientist in Shandong Province (Grant no.: JQ201002) and High-end Foreign Experts Recruitment Programs (Grant Nos.: GDW20143500163, GDW20163500110). Y. Q. Wang would also like to thank the financial support from the Top-notch Innovative Talent Program of Qingdao City (Grant No.: 13-CX-08), the Taishan Scholar Program of Shandong Province, and Qingdao International Center for Semiconductor Photoelectric Nanomaterials and Shandong Provincial University Key Laboratory of Optoelectrical Material Physics and Devices.

References

[1] G.X. Gao, L. Yu, H.B. Wu, X.W. Lou, Hierarchical tubular structures constructed by carbon-coated α-Fe_2O_3 nanorods for highly reversible lithium storage, Small 10 (2014) 1741–1745.
[2] B. Liu, M.H. Cao, X.Y. Zhao, Y. Tian, C.W. Hu, Facile synthesis of ultrafine carbon-coated SnO_2 nanoparticles for high-performance reversible lithium storage, J. Power Sources 243 (2013) 54–59.
[3] F. Han, D. Li, W.-C. Li, C. Lei, Q. Sun, A.-H. Lu, Nanoengineered polypyrrole-coated Fe_2O_3@C multifunctional composites with an improved cycle stability as lithium-ion anodes, Adv. Funct. Mater. 23 (2013) 1692–1700.
[4] B. Wang, J.S. Chen, H.B. Wu, Z. Wang, X.W. Lou, Quasiemulsion-templated formation of α-Fe_2O_3 hollow spheres with enhanced lithium storage properties, J. Am. Chem. Soc. 133 (2011) 17146–17148.
[5] J.J. Zhang, Y.F. Sun, Y. Yao, T. Huang, A.S. Yu, Lysine-assitsted hydrothermal synthesis of hierarchically porous Fe_2O_3 microspheres as anode materials for lithium-ion batteries, J. Power Sources 222 (2013) 59–65.
[6] M.V. Reddy, G.V. Subba Rao, B.V.R. Chowdari, Metal oxides and oxysalts as anode materials for Li ion batteries, Chem. Rev. 113 (2013) 5364–5457.
[7] B. Liu, X.Y. Zhao, Y. Tian, D. Zhao, C.W. Hu, M.H. Cao, A simple reduction process to synthesize MoO_2/C composites with cage-like structure for high-performance lithium-ion batteries, Phys. Chem. Chem. Phys. 15 (2013) 8831–8837.
[8] Z.F. Ma, T.B. Zhao, Reduced graphene oxide anchored with MoO_2 nanorods as anode for high rate and long cycle Lithium ion batteries, Electrochim. Acta 201 (2016) 165–171.
[9] F. Sun, J.H. Gao, H.B. Wu, X. Liu, L.J. Wang, X.X. Pi, Y.F. Lu, Confined growth of small ZnO nanoparticles in a nitrogen-rich carbon framework: advanced anodes for long-life Li-ion batteries, Carbon 113 (2017) 46–54.
[10] X.H. Zhang, X.Y. Qiu, D.B. Kong, L. Zhou, Z.H. Li, X.L. Li, L.J. Zhi, Silicene flowers: a dual stabilized silicon building block for high-performance lithium battery anodes, ACS Nano 11 (2017) 7476–7484.
[11] M. Zhou, X.L. Li, B. Wang, Y.B. Zhang, J. Ning, Z.C. Xiao, X.H. Zhang, Y.H. Chang, L.J. Zhi, High-performance silicon battery anodes enabled by engineering graphene assemblies, Nano Lett. 15 (2015) 6222–6228.
[12] B. Wang, X.L. Li, B. Luo, L. Hao, M. Zhou, X.H. Zhang, Z.J. Fan, L.J. Zhi, Approaching the downsizing limit of silicon for surface-controlled lithium storage, Adv. Mater. 27 (2015) 1526–1532.
[13] Z.Y. Wang, L. Zhou, X.W. Lou, Metal oxide hollow nanostructures for lithium-ion batteries, Adv. Mater. 24 (2012) 1903–1911.
[14] J.X. Guo, L. Chen, G.J. Wang, X. Zhang, F.F. Li, In situ synthesis of SnO_2-Fe_2O_3@polyaniline and their conversion to SnO_2-Fe_2O_3@C composite as fully reversible anode material for lithium-ion batteries, J. Power Sources 246 (2014) 862–867.
[15] Y. Zhao, J.X. Li, N. Wang, C.X. Wu, G.F. Dong, L.H. Guan, Fully reversible conversion between SnO_2 and Sn in SWNTs@SnO_2@PPy coaxial nanocable as high performance anode material for lithium ion batteries, J. Phys. Chem. C 116 (2012) 18612–18617.
[16] X.G. Han, M.S. Jin, S.F. Xie, Q. Kuang, Z.Y. Jiang, Y.Q. Jiang, Z.X. Xie, L.S. Zheng, Synthesis of tin dioxide octahedral nanoparticles with exposed high-energy {221} facets and enhanced gas-sensing properties, Angew. Chem. Int. Ed. 48 (2009) 9180–9183.
[17] C.Z. Wu, P. Yin, X. Zhu, C.Z. OuYang, Y. Xie, Synthesis of hematite (α-Fe_2O_3) nanorods: diameter-size and shape effects on their applications in magnetism, lithium ion battery, and gas sensors, J. Phys. Chem. B 110 (2006) 17806–17812.
[18] Y. Hou, D. Wang, X.H. Yang, W.Q. Fang, B. Zhang, H.F. Wang, G.Z. Lu, P. Hu, H.J. Zhao, H.G. Yang, Rational screening low-cost counter electrodes for dye-sensitized solar cells, Nat. Commun. 4 (2013) 8.
[19] A. Kar, A. Patra, Recent development of core-shell SnO_2 nanostructures and their potential applications, J. Mater. Chem. C 2 (2014) 6706–6722.
[20] B. Zhao, Y.-T. Xu, S.-Y. Huang, K. Zhang, Matthew M.F. Yuen, J.-B. Xu, X.-Z. Fu, R. Sun, C.-P. Wong, 3D RGO frameworks wrapped hollow spherical SnO_2-Fe_2O_3 mesoporous nano-shells: fabrication, characterization and lithium storage properties, Electrochim. Acta 202 (2016) 186–196.
[21] Y.L. Wang, J.J. Xu, H. Wu, M. Xu, Z. Peng, G.F. Zheng, Hierarchical SnO_2-Fe_2O_3 heterostructures as lithium-ion battery anodes, J. Mater. Chem. 22 (2012) 21923.
[22] J. Lin, Z.W. Peng, C.S. Xiang, G.D. Ruan, Z. Yan, D. Natelson, J.M. Tour, Graphene nanoribbon and nanostructured SnO_2 composite anodes for lithium ion batteries, ACS Nano 7 (2013) 6001–6006.
[23] K. Lee, S. Shin, T. Degen, W. Lee, Y.S. Yoon, Insity analysis of SnO_2/Fe_2O_3/RGO to unravel the structural collapse mechanism and enhanced electrical conductivity for lithium-ion batteries, Nano Energy 32 (2017) 397–407.
[24] X.M. Yin, C.C. Li, M. Zhang, Q.Y. Hao, S. Liu, L.B. Chen, T.H. Wang, One-step synthesis of hierarchical SnO_2 hollow nanostructures via self-assembly for high power lithium ion batteries, J. Phys. Chem. C 114 (2010) 8084–8088.
[25] Z.Y. Wang, D.Y. Luan, S. Madhavi, C.M. Li, X.W. Lou, α-Fe_2O_3 nanotubes with superior lithium storage capability, Chem. Commun. 47 (2011) 8061–8063.
[26] Y. Luo, D.D. Yuan, M.S. Balogun, H. Yang, W.T. Qiu, J.C. Liu, P. Liu, Y.X. Tong, Dual doping strategy enhanced the lithium storage properties of graphene oxide binary composites, J. Mater. Chem. A 4 (2016) 13431–13436.
[27] M.S. Balogun, Z.P. Wu, Y. Luo, W.T. Qiu, X.L. Fan, B. Long, M. Huang, P. Liu, Y.X. Tong, High power density nitridated hematite (α-Fe_2O_3) nanorods as anode for high-performance flexible lithium ion batteries, J. Power Sources 308 (2016) 7–17.
[28] Y. Yu, C.-H. Chen, Y. Shi, A tin-based amorphous oxide composite with a porous spherical, multideck-cage morphology as a highly reversible anode material for lithium-ion batteries, Adv. Mater. 19 (2007) 993–997.
[29] L. Hu, Y.M. Huang, F.P. Zhang, Q.W. Chen, CuO/Cu_2O composite hollow polyhedrons fabricated from metal-organic framework templates for lithium-ion battery anodes with a long cycle life, Nanoscale 5 (2013) 4186–4190.
[30] Y.Q. Fu, Q.L. Wei, X.Y. Wang, H.B. Shu, X.K. Yang, S.H. Sun, Porous hollow α-Fe_2O_3@TiO_2 core-shell nanospheres for superior lithium/sodium storage capability, J. Mater. Chem. A 3 (2015) 13807–13818.
[31] M.S. Balogun, C. Li, Y.X. Zeng, M.H. Yu, Q.L. Wu, M.M. Wu, X.H. Lu, Y.X. Tong, Titanium dioxide@titanium nitride nanowires on carbon cloth with remarkable rate capability for flexible lithium-ion batteries, J. Power Sources 272 (2014) 946–953.
[32] K. Chang, W.X. Chen, L-cysteine-assisted synthesis of layered MoS_2/Graphene composites with excellent electrochemical performances for lithium ion batteries, ACS Nano 5 (2011) 4720–4728.
[33] Y. Wang, H.C. Zeng, J.Y. Lee, Highly reversible lithium storage in porous SnO_2 nanotubes with coaxially grown carbon nanotube overlayers, Adv. Mater. 18 (2006) 645–649.
[34] M.S. Balogun, W.T. Qiu, J.H. Jin, Y.C. Huang, Y. Luo, H. Yang, C.L. Liang, X.H. Lu, Y.X. Tong, Vanadium nitride nanowire supported SnS_2 nanosheets with high reversible capacity as anode material for lithium ion batteries, ACS Appl. Mater. Interfaces 7 (2015) 23205–23215.
[35] M.S. Balogun, W.T. Qiu, Y. Luo, Y.C. Huang, H. Yang, M.Y. Li, M.H. Yu, C.L. Liang, P.P. Fang, P. Liu, Y.X. Tong, Improving the lithium-storage properties of self-grown nickel oxied: a back-up from TiO_2 nanoparticles, ChemElectroChem 2 (2015) 1243–1248.
[36] Z.X. Yang, H.Y. Wang, W.J. Song, W. Wei, Q.P. Mu, B. Kong, P.Q. Li, H.Z. Yin, One dimensional SnO_2 NRs/Fe_2O_3 NTs with dual synergistic effects for photoelectrocatalytic reduction CO_2 into methanol, J. Colloid Interface Sci. 486 (2017) 232–240.
[37] X.S. Zhou, L.-J. Wan, Y.-G. Guo, Bingding SnO_2 nanocrystals in nitrogen-doped graphene sheets as anode materials for lithium-ion batteries, Adv. Mater. 25 (2013) 2152–2157.
[38] V. Etacheri, Gulaim A. Seisenbaeva, J. Caruthers, G. Daniel, J.-M. Nedelec, Vadim G. Kessler, Vilas G. Pol, Ordered network of interconnected SnO_2 nanoparticles for excellent lithium-ion storage, Adv. Energy Mater. 5 (2015) 1401289.
[39] H. Liu, G.X. Wang, J. Park, J.Z. Wang, H.K. Liu, C. Zhang, Electrochemical performance of α-Fe_2O_3 nanorods as anode material for lithium-ion cells, Electrochim. Acta 54 (2009) 1733–1736.
[40] X. Wang, Y. Xiao, C.W. Hu, M.H. Cao, Adual strategy for improving lithium storage performance, a case of Fe_2O_3, Mater. Res. Bull. 59 (2014) 162–169.
[41] W.W. Zhou, C.W. Cheng, J.P. Liu, Y.Y. Tay, J. Jiang, X.T. Jia, J.X. Zhang, H. Gong, H.H. Hng, T. Yu, H.J. Fan, Epitaxial growth of branched α-Fe_2O_3/SnO_2 nano-heterostructures with improved lithium-ion battery performance, Adv. Funct. Mater. 21 (2011) 2439–2445.